JOURNAL OF MATERIALS SCIENCE **37** (2002) 4333–4341

Modelling the structure changes in quenchable steel subjected to grinding

I. ZARUDI, L. C. ZHANG*
School of Aerospace Mechanical and Mechatronic Engineering, The University of Sydney, NSW 2006, Australia
E-mail: zhang@mech.eng.usyd.edu.au

This paper analyzes the consequences of the microstructural changes in a quenchable steel component subjected to grinding. The model takes into account the coupling of the temperature history and stress field in the grinding, where the temperature field is assessed by Jager's model and the stress field is analyzed by means of an embossed grid method. The effects of the dislocation density and grain size distribution are also examined. The transformation kinetics of martensite, bainite and ferrite is then discussed based on the Cahn's law. It was found that that the temperature-stress field varies significantly in different subsurface parts of the component and thus creates a variable structure across its depth. The theoretical results are in good agreement with experimental data.

1. Introduction

A recent study showed the surface grinding could enhance the mechanical properties of a quenchable steel component [1], in which the structural changes in the subsurface such as phase transformation plays a key role [2]. Thus to control the grinding-induced surface treatment process, the prediction of the component's subsurface structure is important.

To the authors' knowledge, no attempt has been made to model the structural transformations during surface grinding, where the effects of temperature rise and mechanical stresses are coupled. However, there exist a number of studies on the phase transformation events in grinding, discussing the methods of eliminating subsurface damages. For example, Shaw considered the white layers in grinding as the untempered martensite and discussed its formation by taking into account the rate of carbon diffusion [3]. Eda and co-authors studied the temperature rise in subsurface and carbon redistribution [4], and concluded that the ground layer is composed of α-phase, fine recristalized γ-phase and secondary carbides. Tomilin analyzed the effects of workpiece speed and grinding-wheel condition on the thickness of the transformation zone [5]. Zhang and co-authors [6, 7] showed that under some specified distributions of heat flux, convection process of coolants and properties of work materials, the depth and nature of subsurface phase change and the distribution of residual stresses can be described quantitatively with respect to the material removal rate and coolant application method. In all works specified above, however, the mechanism of the martensite phase evolution in terms of the materials' microstructure has not been discussed. The details of stress state variation and cooling conditions across the layer depth were also lacking.

The process of the surface modification by grinding can be viewed as a certain case of the thermo-mechanical treatment (TMT) with high stress and high strain rate during deformation, and there have been some related studies on TMT [8–12]. Majta [8] mentioned that the thermo-mechanical history in a component could alter its final structure. Liu and co-authors [9] studied the changes of the transformation kinetics of the deformed austenite due to the increase of dislocation density, and established a model of phase transformation from austenite to ferrite, pearlite and bainite of hot deformed steel based on the Cahn's transformation theory. The model was improved by Qu [10] by taking into account the cooling rate and chemical composition of the system. Denis offered a complicated model considering temperature and stress fields, chemical composition and phase transformation during heat treatment [12].

The present paper aims to model the phase transformation events in surface grinding in a new way. The process will be considered as the combination of grinding and TMT with a moving heat flux. The effects of cooling rate, stress history, dislocation density and grain boundary interaction will be discussed. Although only one type of steel was studied in the present work the method might be applied to other quenchable steels, e.g., that could be hardened by means of martensite phase transformation.

2. Experiment

The testing material selected was a widely used steel, AISI 4140, initially tempered with micro hardness of $HV_{(300g)} = 350$. The chemical composition of the steel is listed in Table I.

*Author to whom all correspondence should be addressed.

TABLE I Chemical composition of the AISI 4140 steel

Chemical element	Fe	C	Si	Mn	Cr	Mo
%	Balance	0.40	0.25	0.80	0.90	0.20

TABLE II Grinding conditions

Grinding mode	Up-grinding
Workpiece material	AISI 4140
Grinding wheel	A120MVAA
Wheel diameter (mm)	280
Wheel speed (m/s)	27
Grinding width (mm)	15
Table speed (m/min)	0.2
Depth of cut (μm)	105

TABLE III Wheel dressing conditions

Type of dresser	Single-point diamond
Wheel speed (m/min)	10
Dressing, cross-feed rate (mm/revolution)	0.1

The grinding was performed on a surface grinder, Minini Junior 90 CF CNC M286, with the grinding parameters listed in Tables II to III in an up-grinding mode. A 3-component 'Kistler' dynamometer of Type 9257B was used to measure the grinding forces.

A temperature measuring system composed of an optical microscope, a CCD camera and a video recorder was used to establish the temperature field in the subsurface of the treated component. The detailed description of the method could be found in [13]. The temperature field was analyzed by an image analysis system, Leica Qwin.

The stress field in the subsurface of the components was determined with the aid of an embossed grid method described in [14]. The surface of the sample perpendicular to the surface to be ground was first polished by the method shown in Ref. [15]. An array of orthogonal lines on the polished surface was then generated using a CNC milling machine. The initial grid (Fig. 1) was with a density of 10 lines per millimeter and each line had a thickness of 16 μm. The deformation of the grid during grinding was recorded continuously with the aid of the video recorder. The deformed grid was then superimposed on the undeformed one to work out the relative point-wise displacements caused by grinding. The corresponding strain components were determined using the method described in Refs. [14, 16].

The depth of the subsurface layer experienced structural changes after grinding was checked on the cross-section view samples by an optical microscope. The microstructure of the layer was characterized by a transmission electron microscope (TEM), CM12 (Philips). To this end, plan view samples were prepared for different parts of the layer. The plane perpendicular to the ground surface was polished and etched. In this way the bottom of the hardened layer was revealed. Then, different amount of material was removed from the ground surface by lapping to obtain the samples in the required parts of the layer. In the above preparation, the temperature throughout a specimen was kept below 40°C to ensure that no micro-structural changes took place.

3. Theoretical analysis

3.1. Temperature rise in subsurface

In grinding, since a workpiece is moving with a constant speed, the surface heating due to grinding can be viewed as a moving heat flux. Thus the Jager's model [17] can

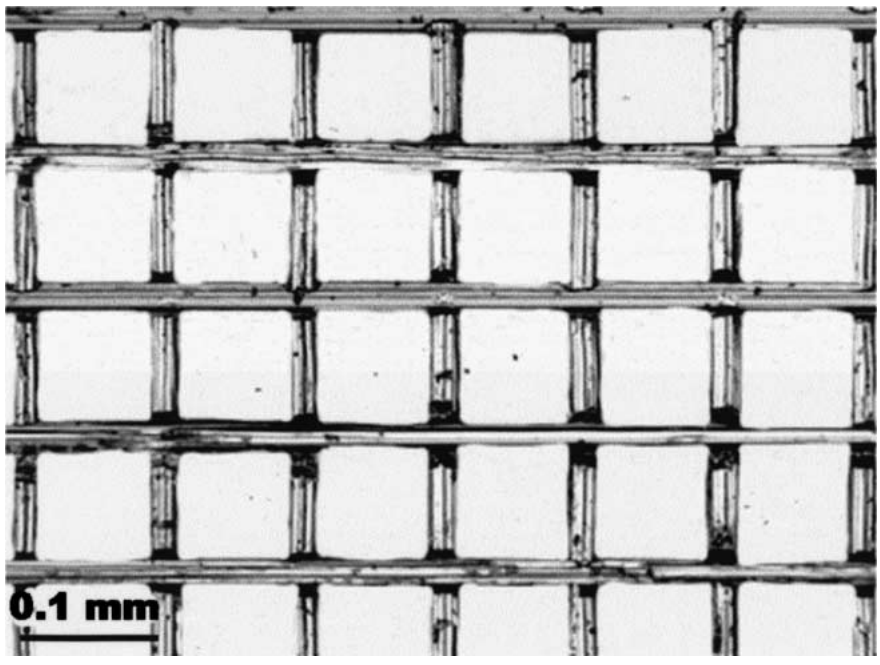

Figure 1 The initially embossed grid.

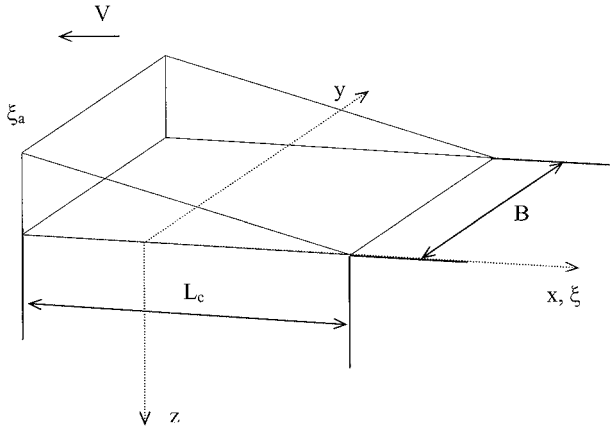

Figure 2 A schematic model for a surface heat source.

be used to calculate the steady-state temperature rise, $\bar{T}(X, Z)$ in the workpiece, i.e.,

$$\bar{T}(X, Z) = \int_{X-L}^{X+X_a} \mathrm{e}^{-\eta} K_0(|\eta|)\,\mathrm{d}\eta - \int_{X-B}^{X+B} \times \mathrm{e}^{-\eta}\,\mathrm{d}\eta \int_B^{\infty} \frac{\mathrm{e}^{-(\eta^2+\varsigma^2)^{1/2}}}{(\eta^2+\varsigma^2)^{1/2}}\,\mathrm{d}\varsigma \quad (1)$$

where

$$\bar{T}(X) = \frac{\pi K V}{2\chi q} T(X, Z), \quad (2)$$

K is the conductivity of the workpiece material, ρ is the density, c is the specific heat, K_0 is the modified Bessel function of the second kind of order zero,

$$\chi = \frac{K}{\rho c} \quad (3)$$

and X, L and B are non-dimensional parameters defined by

$$X = \frac{Vx}{2\chi}, \qquad L = \frac{VL_c}{2\chi}, \qquad B = \frac{Vb}{2\chi}$$
$$Z = \frac{Vz}{2\chi}, \qquad X_a = \frac{V\xi_a}{2\chi}. \quad (4)$$

In the above equation, x, y and z are the current coordinates and L_c, b and ξ_a are defined in Fig. 2.

Our recent studies [13] showed that a triangular heat flux with $\xi_a = 1$ gives the best fit to the up-grinding experiment used in this study. Thus in the following analysis we will take $\xi_a = 1$.

3.2. Heat conduction

The field of temperature rise established above was then used to assess cooling in grinding.

The governing differentiation equation for this purpose can be written as [18]:

$$\frac{\partial^2 T}{\partial x^2} + \frac{\partial^2 T}{\partial y^2} + \frac{\partial^2 T}{\partial z^2} + \frac{\dot{q}}{K} = \frac{1}{a}\frac{\partial T}{\partial \theta} \quad (5)$$

where θ is time, T is temperature, α is thermal diffusivity of the work material and $\dot{q}$ is the surface heat flux induced by grinding.

Along the grinding surface, the Neuman boundary condition is used, i.e.,

$$-K\left(\frac{\partial T}{\partial x}n_x + \frac{\partial T}{\partial y}n_y + \frac{\partial T}{\partial z}n_z\right) = h(T - T_\infty) \quad (6)$$

where h is the heat transfer coefficient, and in the workpiece far away from the grinding zone, the temperature T_∞ is 20°C.

The problem was solved by the finite-difference method.

3.3. Phase transformations

The possible phase transformation events were analyzed with the aid of the Cahn's phase transformation theory and Sheil's additive rule in accordance with Ref. [9]. In the analysis we assumed that the transformation to austenite (γ) took place as the temperature rise exceeded 800^0C. All the possible phase transformations on cooling to ferrite (α), perlite, bainite and martensite were then investigated. To consider the effect of the austenite deformation on the transformation kinetics, the dislocation density and grain size of the phase need to be examined.

At the early stage of $\gamma \rightarrow \alpha$ transformation, the mechanism of growth and nucleation takes place [9] when

$$\frac{\mathrm{d}X_{F_1}}{\mathrm{d}t} = 4.046(I_S S_\gamma)^{0.25} G_F^{0.25} \left(\ln\frac{1}{1-x}\right)^{0.75} (1 - X) \quad (7)$$

where X_{F_1} is the transformation fraction of a phase, X is the total transformed fraction, S_γ is the surface area of γ grains in unit volume, G_F is the growth rate of α, I_S is the nucleation rate of α and

$$I_S = K_1 T^{-0.5} D_c \exp\left(\frac{K_2}{RT\Delta G_V^2}\right) \quad (8)$$

is a function of D_c, the diffusivity of carbon in γ (taken according to Ref. [19]), ΔG_V, the free energy change in unit volume for the nucleation of α phase [19], T, the absolute temperature, R, and gas constant. In Equation 8 K_1 and K_2 are constants, where K_1 was taken as 476.5 cm $\mathrm{K}^{-1/2}$ and K_2 as 1.14 10^9 $\mathrm{J}^3/\mathrm{mol}^3$ [9].

The site saturation model for ferrite and perlite transformation were ignored as only a very low amount of ferrite (as will be shown later) was formed.

During a continuous cooling, the austenite to bainite transformation was determined by

$$\frac{\mathrm{d}X_B}{\mathrm{d}t} = K_3 S\gamma G_F (1 - X) \quad (9)$$

where X_B is the transformed fraction of bainite, K_3 is the coefficient that was taken as $K_3 = 6.816 \times 10^{-4} \exp(\frac{3431.5}{T})$ according to Ref. [20].

3.4. Grain size

The austenite grain size significantly adjusts the kinetics of the phase transformation and alters the value of $S\gamma$. The equation describing the austenite grain size (D_γ) during deformation [21] can be written as

$$D_\gamma = M_0^r \varepsilon^{-m} \tag{10}$$

where $r = 0.67$ and $m = 0.67$ are coefficients and ε is an effective plastic strain of the material.

3.5. Dislocation density

The variation of the dislocation density changes the thermodynamic balance of the phase transformation events. The deformation of austenite at elevated temperatures increases its free energy and such an increase could be expressed as [9]

$$\Delta\mu^d = \frac{1}{2}\mu b^2 \rho V_\gamma \tag{11}$$

where μ is the shear modulus of the γ phase, b is the Burgers vector of a dislocation, V_γ is the Molar volume of the gamma phase and ρ is the dislocation density of austenite determined by [22]

$$\rho = \rho_0 + C\varepsilon_{ef}^g \tag{12}$$

where ρ_0 is the initial dislocation density, ε_{ef} is the effective plastic strain and $C = 2 \times 10^9$ cm^{-2} and $g = 0.7$ are constants.

4. Results and discussion

4.1. The field of temperature rise and cooling history

Fig. 3 shows the experimental and theoretical results of the instant temperature rise field, which are in good agreement. The field is asymmetric in shape with the maximum temperature rise at the sample surface. In the vertical direction across the subsurface the gradient of the field is sharp. The maximum depth of the temperature rise to 800°C (the threshold for $\alpha \rightarrow \gamma$ transformation) is 1.05 mm, correlating well with the depth of the hardened layer formed in the process. The movement of the heated zone was stable, leading to a quite uniform hardened layer and good surface integrity.

The material in different parts of the subsurface layer experiences different cooling rates as presented in Fig.4. The cooling curves vary with the depth of the hardened layer. The top surface of the component undergoes the maximum temperature rise to 1020°C, followed by the high cooling rate more than 100°C/s, so that it reaches the martensite transition temperature in 4 s. The temperature rise decreases in deeper subsurface of the layer and so does the cooling rate. At the

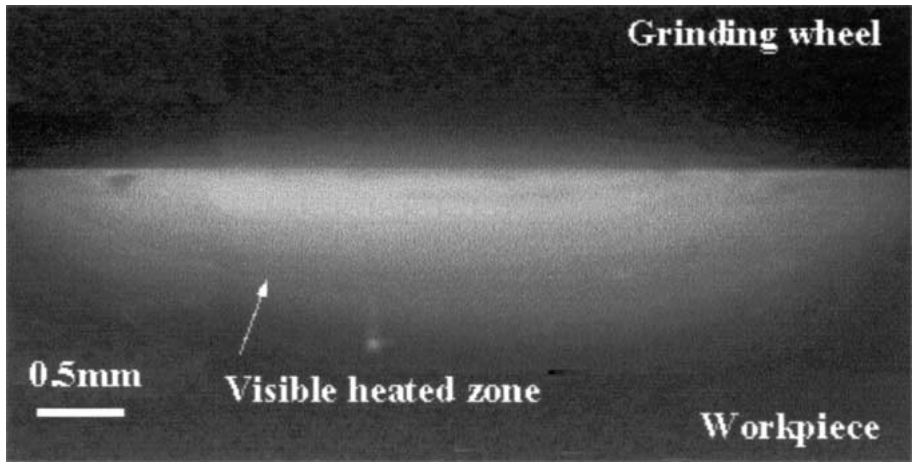

(a)

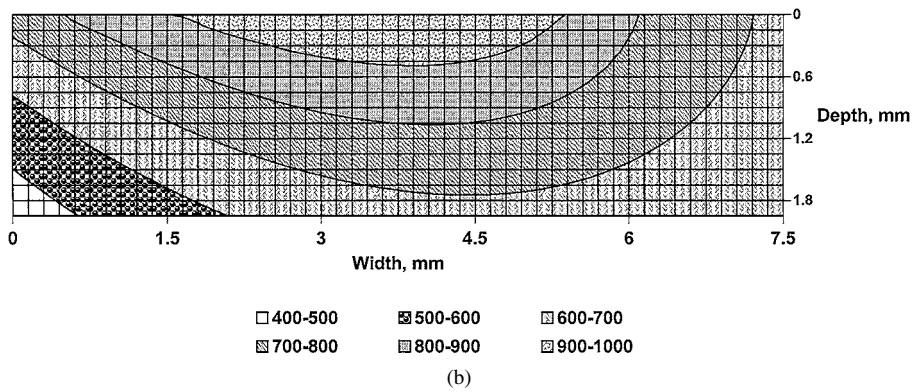

(b)

Figure 3 The temperature rise in the subsurface of the component during surface grinding (depth of cut = 105 μm, infeed velocity = 0.2 m/min) (a) experiment and (b) theory.

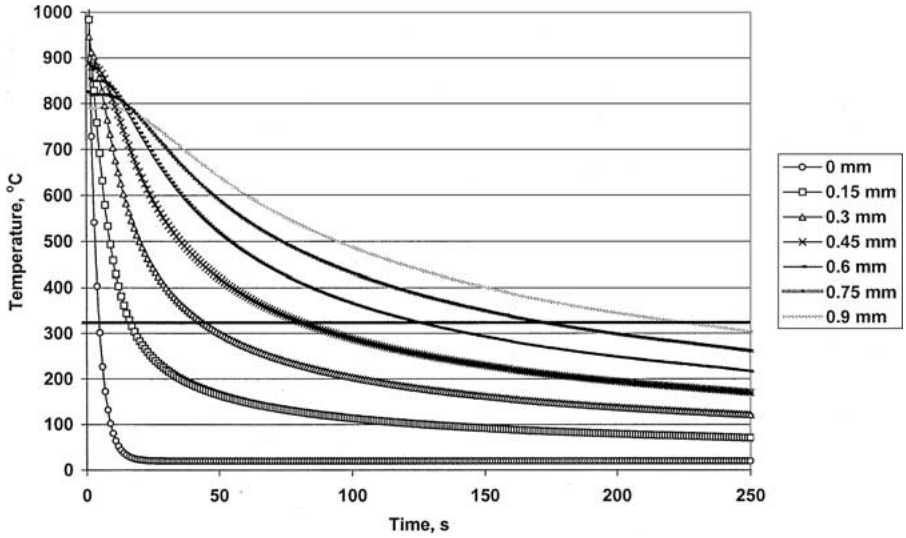

Figure 4 The cooling history in different parts of the grinding-induced hardened layer.

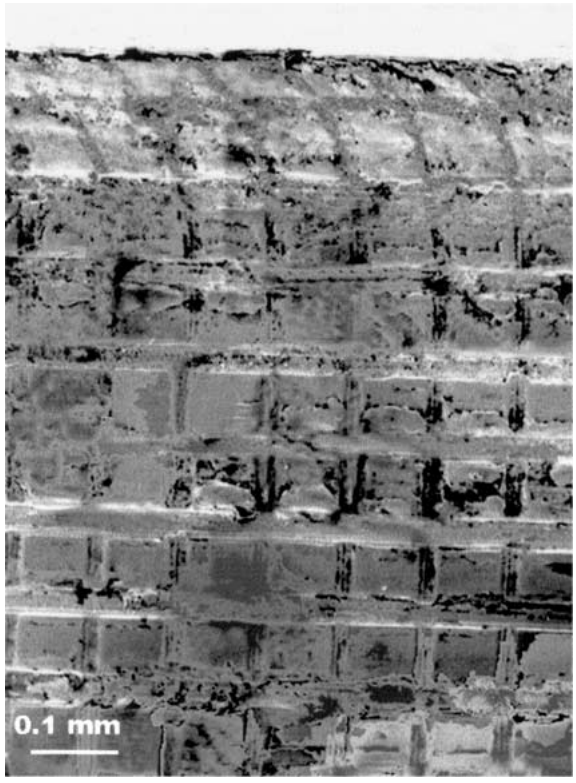

Figure 5 Deformed grid after grinding.

depth of 0.75 mm, for example, the temperature rise approaches 825°C and the cooling rate falls to 4°C/s. The effect of the cooling rate on the transformation kinetics will be discussed in Section 4.5.

4.2. Strain distribution

The deformed grid is shown in Fig. 5. The main distortion of the grit occurred in the first three rows. As shown in Fig. 6, the shear strain (γ_{xy}) at the sample surface is very high, decreases rapidly with the depth of the layer and becomes negligible at the depth of 0.45 mm. The normal strain parallel to the grinding direction (ε_{xx}) is tensile at the surface. However, decreases with the increase in depth beneath the surface and disappears at the depth of 0.25 mm. The normal strain perpendicular to the grinding direction (ε_{yy}) is also tensile at the surface but becomes negative just beneath it and approaches zero when the depth increases further. All strains become negligible at the depth of 0.8 mm under the surface.

TABLE IV Effective plastic strain, grain size and dislocation density of the hardened layer

Depth (μm)	Effective strain (%)	Austenite grain size (μm)		Dislocation density (11) cm^{-1}
		Theory	Experiment	
0	93	3.9	6	2×10^9
150	32	9.4	10	10^9
300	13	20	15	6×10^8
450	7	50		4×10^8
600	3	60		3×10^8
750	1	60		2×10^8
900	0.08	60		10^8

The variation of the effective strain, which is defined as

$$\bar{\varepsilon} = \sqrt{\frac{2}{3}}\sqrt{\varepsilon_{xx}^2 + \varepsilon_{yy}^2 + \frac{\gamma_{xy}^2}{2}} \tag{13}$$

is listed in Table IV. It is clear that the effective strain reaches its maximum at the surface, diminishes swiftly in the subsurface and becomes negligible at the depth of 0.75 mm.

4.3. Grain size and dislocation density

The variations of the grain size and dislocation density in the subsurface can now be calculated using Equations 10 and 12, respectively. The results are presented in Table IV. The theoretical grain size of the deformed austenite is significantly refined at the top

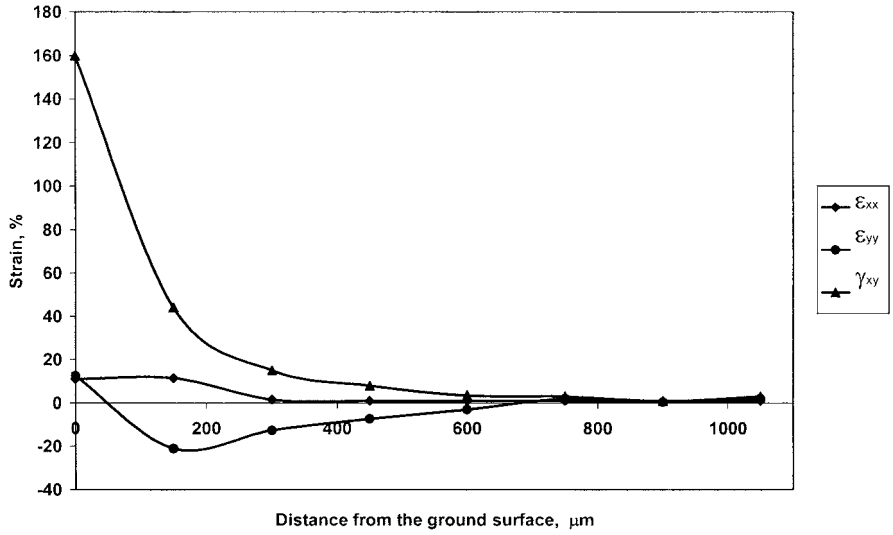

Figure 6 Distribution of the residual plastic strain in the subsurface region after surface grinding.

of the hardened layer. The size increases progressively towards the bottom of the layer. Austenite grain size was also determined experimentally by means of the transmission electron microscopy as the austenite grain boundaries could be resolved even after martensite transformation. The experimental value of the grain size at the top layer is in good agreement with the theoretical. The austenite grain size at the bottom parts of the layer was too large for the TEM to distinguish. In addition to the grain size variation, it has also found that the dislocation density in the top parts of the layer has increased by an order, as shown in Table IV.

4.4. Microstructure of the hardened layer

Fig. 7 shows the microstructure of the subsurface of a ground component. The top part of the layer (Fig. 7a) is composed of refined martensite crystals. No carbides are located. However, carbides can be located inside some of the laths (Fig. 7b and c) at the depth of 0.45 mm. This indicates that the low bainite started to form in these parts of the layer along with the martensite. As the depth of the layer increases further, the number of laths containing carbides increases, indicating the development of the bainite phase. Carbides could be located not only inside the laths but also at its boundaries (Fig. 8a), demonstrating the formation of high bainite in the bottom parts of the hardened layer. The details of the carbide formation at the laths boundaries can be seen in Fig. 8b and c.

4.5. Transformation kinetics

To establish the kinetics of the phase transformation events we first applied Scheil's additive rule to calculate the starting temperature of transformation [23] for possible phases. Then the Cahn's phase transformation theory was employed and the amount of the transformed phase was obtained by using Equations 8 and 9. The results showed that no ferrite precipitation in the layer to the depth of 0.9 mm with starting transformation temperature of 645°C. However, bainite emerges at the depth of 0.3 mm with bainite starting temperature rising for deeper parts of the layer (see Fig. 9a for details). The bainite starting temperature rises from 450°C to 522°C as the depth deviates from 0.3 mm to 0.9 mm due to the low cooling rates in the deeper parts of the layer.

The transformation amount of ferrite and bainite in different parts of the layer is presented in Fig. 9b. The traces of the ferrite can be only found at the bottom of the layer (2% at depth of 0.9 mm). Three input parameters are influencing the ferrite transformation kinetics-austenite grain size, dislocation density and cooling rate. The grain size refinement and the higher dislocation density in the top part of the hardened layer promote the austenite-ferrite transformation, while the high cooling rate suppresses it. However, the high cooling rate must have a dominant effect because no ferrite is formed almost along the whole depth of the hardened layer. The formation of bainite, nevertheless, takes place at a depth of 0.3 mm, but the top part of the layer is bainite free. The bainite starting temperature for the upper parts of the layer is reduced due to the high cooling rate there, leading to the formation of a limited amount of "low" bainite. The rise starting temperature of the bainite promotes the "high" bainite. The amount of bainite increases to 92% at the depth of 0.9 mm.

It is assumed that all the untransformed austenite will undergo martensite transformation at 310°C. As can be seen from Fig. 9b, martensite occupies 100% of the subsurface down to the depth of 0.15 mm and remains a dominant phase towards the middle of the layer. The martensite diminishes in the deeper subsurface due to increasing bainite. The mixture of the martensite and bainite dominates the lower parts of the layer with a bainite supremacy at the bottom of the layer.

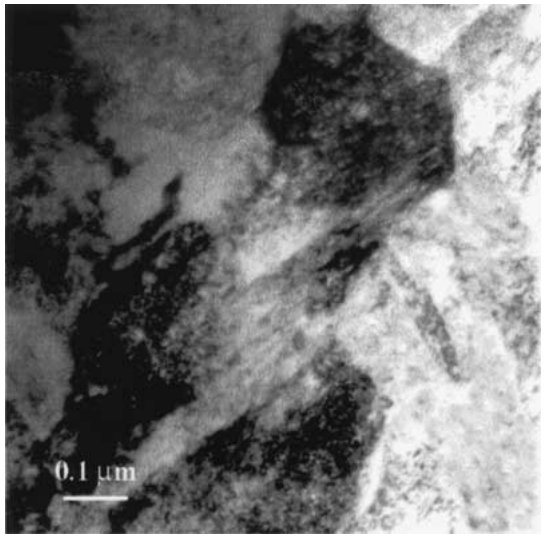

(a)

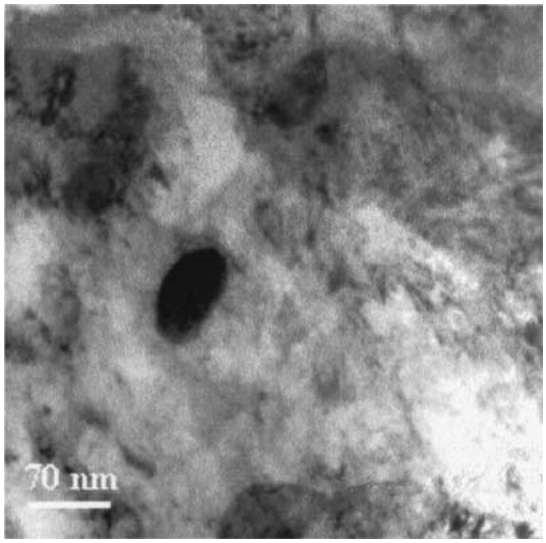

(b)

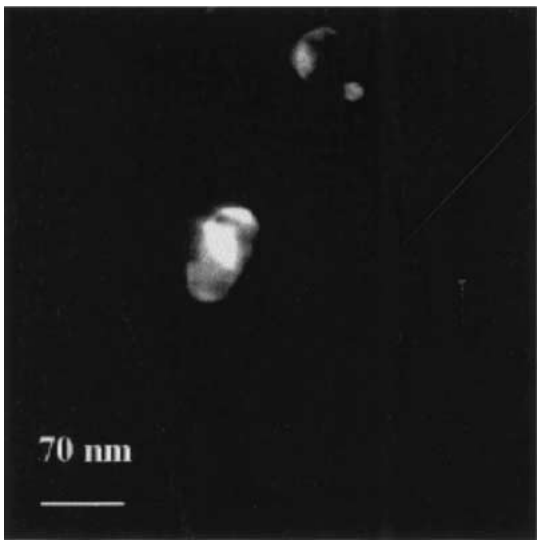

(c)

Figure 7 The microstructure of the subsurface material at different depths from ground surface (a) depth = 0.15 mm. Note the refined martensite laths and the absence of carbide, (b) depth = 0.3 mm (the bright field image). Note the intralaths carbides in low bainite; (b) is the dark field image of (a) $g = 1\bar{1}0$ of carbide.

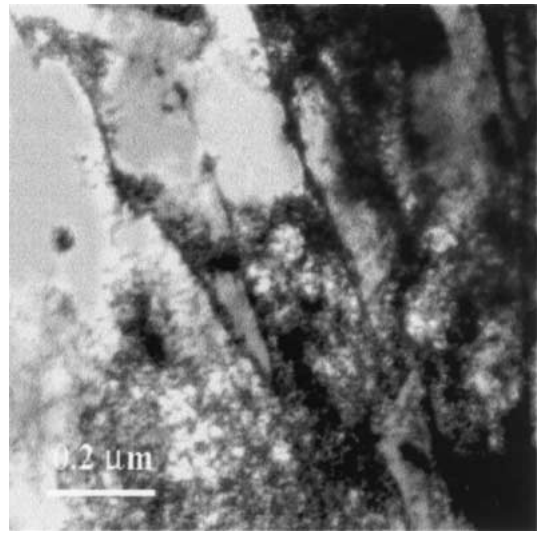

(a)

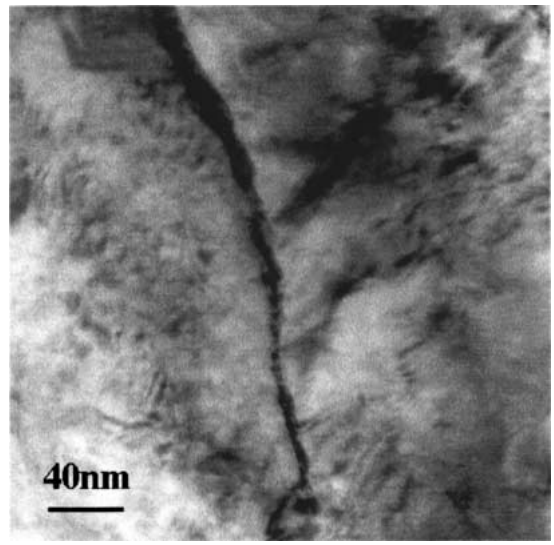

(b)

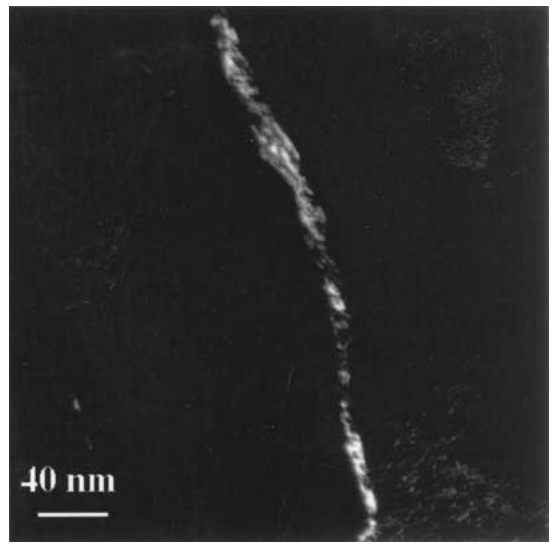

(c)

Figure 8 Bainite of the subsurface material at various depths from the ground surface (a) depth = 0.6 mm. Note the intralaths and interlaths carbide in upper bainite; (b) the bright field image of the inter laths carbide at depth = 0.72 mm; (c) is the dark field image of (b) g = 123 of carbide.

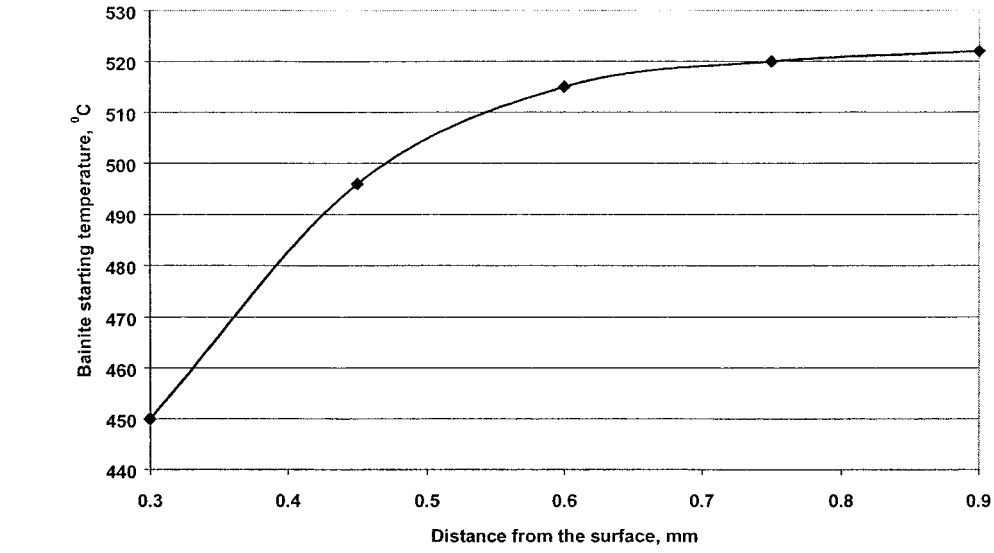

(a)

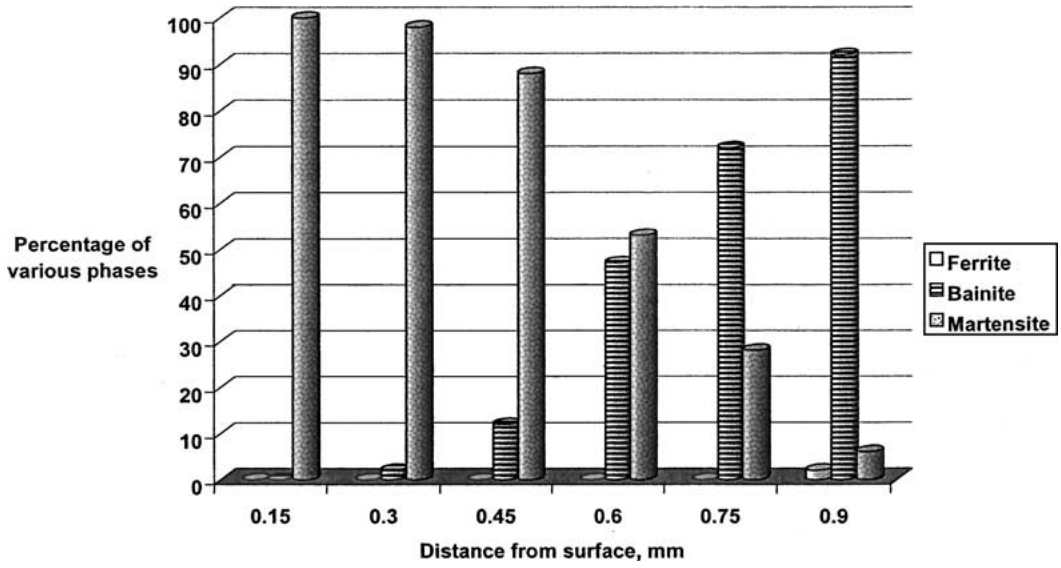

(b)

Figure 9 (a) The bainite starting temperature in different parts of the hardened layer, (b) The theoretical phase composition in different parts of the hardened layer.

5. Conclusions

Cooling history, stress state, dislocation density, grain size and their combinations dramatically alter the transformation kinetics and structure of the subsurface layer of a component subjected to grinding.

The high cooling rates at the top part of the layer suppress the formation of ferrite and bainite. At the same time, the high degree of deformation refined the austenite grains, leading to a fine-grained martensite. The experimental findings did confirmed that at the top subsurface the martensite grains were very much refined. Due to the reduction of the cooling rate and degree of deformation in the deeper subsurface, bainite appears but its starting temperature becomes rather low. Nevertheless, the deformation of the layer and the comparatively small size of the deformed austenite (Table IV) accelerate the growth rate of bainite. As a result a low bainite emerges in the upper parts of the layer with its amount rising to the bottom of the layer. The "low" bainite was proved experimentally as intralaths bainite [24]. In the bottom part of the layer the cooling rate decreases further, allowing formation of upper bainite with a higher starting temperature. However, the growth rate of bainite is not very much affected by the stress state as the deformation is negligible at the bottom part of the layer. Again the "high" bainite was verified as the interlaths bainite [24].

In short, the hardened layer induced by grinding has a complicated variable structure composed of fine-grained martensite at the ground surface with a graduall transition to bainite along the depth.

Acknowledgments

The authors wish to thank the Australian Research Council (ARC) for continuing support of this project and the Electron Microscope Unit of Sydney University for use of its facilities.

References

1. I. ZARUDI and L. C. ZHANG, *J. Mater. Sci.* **37**(18) (2002) 3935.

2. *Idem*., in "applied Mechanics: Progress and Application" (World Scientific, Singapore, 2002).
3. M. C. SHAW and A. VYAS, *Annals of the CIRP* **43** (1994) 279.
4. H. EDA, E. OHMURA, S. YAMAUCHI and I. INASAKI, *CIRP Annals* **42** (1993) 389.
5. W. J. TOMLINSON, L. A. BLUNT and S. SPRAGGETT, *Journal of Materials Processing Technology* **25** (1991) 105.
6. L. ZHANG and M. MAHDI, *International Journal of Machine Tools & Manufacture* **35** (1995) 1397.
7. M. MAHDI and L. ZHANG, *ibid.* **38** (1998) 1289.
8. J. MAJTA, J. G. LENARD and M. PIETRZYL, *Material Science and Engineering* A **208** (1996) 249.
9. Z. LIU, G. WANG and W. GAO, *Journal of Materials Engineering and Performance* **5** (1996) 521.
10. J. QU, Z. LIU and G. WANG, *Journal of Materials Science Technology* **14** (1998) 380.
11. M. UMEMOTO, H. OHTSUKA and I. TAMURA, *Transactions ISIJ* **23** (1983) 775.
12. S. DENIS, C. ARCHAMBAULT, C. AUBRY, A. MEY, J. C. LOUIN and A. SIMON, *Journal de Physique* IV **9** (1999) 323.
13. I. ZARUDI and L. ZHANG, *International Journal of Machine Tools & Manufacture* **42**(8) (2002) 905.
14. J. A. BAILEY and S. JEELANI, *Wear* **36** (1976) 199.
15. L. C. ZHANG and I. ZARUDI, *ibid.* **225–229** (1999) 669.
16. D. W. WU, *ibid.* **147** (1991) 311.
17. J. JAEGER, *Journal and Proc. of the Royal Society of NSW* **76** (1942) 203.
18. F. KREITH, "Principles of Heat Transfer" (Intext Educational Publishers, New York, 1973).
19. M. ENOMOTO and H. I. AARONSON, *Metallurgical Transactions* A **17A** (1986) 1385.
20. M. SUEHIRO, T. SENUMA, H. YADA, and K. SATO, *ISIJ International* **32** (1992) 433.
21. C. M. SELLARS, in "Deformation, Processing and Structure," ASM Materials Science Seminar (ASM, Metals Park, OH, 1982) p. 245.
22. G. T. HAHN, *Acta metallurgica* **10** (1962) 727.
23. J. W. CHRISTIAN, "The Theory of Transformations in Metals and Alloys" (Pergamon Press, Oxford, 1975).
24. B. L. BRAMFITT and J. G. SPEER, *Metallurgical Transactions* A **21A** (1990) 817.

Received 13 December 2001
and accepted 20 June 2002